Photoelectrochemical Fabrication of CuO-Cu_2O Nanocomposite Semiconductors by High-Frequency Potential-Switching in Copper(II)-Tartrate Complex Aqueous Solution and the Energy Band Structures

To cite this article: Shinichi Yamamoto *et al* 2023 *J. Electrochem. Soc.* **170** 032505

Journal of The Electrochemical Society, 2023 **170** 032505

Photoelectrochemical Fabrication of CuO-Cu_2O Nanocomposite Semiconductors by High-Frequency Potential-Switching in Copper (II)-Tartrate Complex Aqueous Solution and the Energy Band Structures

Shinichi Yamamoto,[1] Ryoga Yokoyama,[1] Kosuke Imahori,[1] Pei Loon Khoo,[1] Natsuko Asano,[2] Shunsuke Asahina,[2] Tsutomu Shinagawa,[1,3] and Masanobu Izaki[1,*,z]

[1]*Graduate School of Engineering, Toyohashi University of Technology, Toyohashi-shi 441-8580, Japan*
[2]*EP Application Department, EP Business Unit, JEOL Ltd., Tokyo 196-8558, Japan*
[3]*Electronics Materials Divisions, Morinomiya Center, Osaka Research Institute of Industrial Science and Technology, Osaka 536-8553, Japan*

P-type CuO-Cu_2O nanocomposite semiconductors composed of Cu_2O-embedded CuO aggregations and Cu_2O aggregation consisting of space-filling CuO grains have been fabricated by photoelectrochemical high-frequency potential-switching of 100 to 1000 cycles in an aqueous solution containing copper(II) sulfate hydrate, tartaric acid, and sodium hydroxide, and the size of both the CuO and Cu_2O grains decreased from 40–44 nm to approximately 10 nm remaining the characteristic monoclinic and cubic lattices with an increase in cycle numbers. The bandgap energy of CuO components was almost a constant value of 1.5 eV, and the Cu_2O components showed a decrease in bandgap energy from 2.05 eV to 1.85 eV with an increase in cycle number due to the Cu^{2+} state incorporation, and the CuO-Cu_2O nanocomposites possessed an ionization energy of approximately 5.2 eV and work function of approximately 4.6 eV respectively, and were close to those for single CuO and Cu_2O layers.
 [DOI: 10.1149/1945-7111/acb616]

Manuscript submitted September 27, 2022; revised manuscript received January 11, 2023. Published March 15, 2023.

Supplementary material for this article is available online

The efficient use of bountiful solar energy reaching Earth is an indispensable way to realize a CO_2-free sustainable society for the benefit of all living things.[1] Solar energy can be converted into electricity and hydrogen gas by using photovoltaic processes in semiconductors and devices such as solar cells[2] and photocathodes for photoelectrochemical water splitting.[3] The photovoltaic conversion process is composed of (i) the absorption of light of photon energy larger than the bandgap energy, (ii) the formation of excitons of hole-electron pair, (iii) the dissociation of excitons to free carriers, and (iv) the transportation of free carriers by the electric field formed at the heterointerface.[4–6] The conversion efficiency of a single p/n-heterojunction solar cell is limited at approximately 30% by the Shockley–Queisser Limit under AM1.5 G and 1 Sun condition.[7] Multi-junction tandem solar cells[8] and quantum dots solar cells[2] have been proposed to overcome the efficiency limit of single-junction solar cells by a strategy of containing two or more p-type semiconductors with different bandgap energies, and a high performance of 39.2% has been demonstrated by a six-junction III-V solar cell under 1Sun.[9]

Cu_2O and CuO are p-type semiconductors with bandgap energies of 2.0 eV and 1.5 eV,[10,11] respectively. They have been employed as photovoltaic layers in solar cells,[12,13] and as photocathodes to generate hydrogen gas from water by irradiating Sunlight.[14] Also, the Cu_2O/CuO bilayers and CuO-Cu_2O nanostructures have attracted increasing attention as high-performance photovoltaic materials which satisfy the aforementioned strategy to realize high conversion efficiency.[15–18] The single layers, bilayers, and nanostructures of CuO and Cu_2O have been prepared by several techniques of thermal oxidation of precursors,[19,20] gas-phase deposition processes, and solution electrochemical process,[21,22] but high-temperature thermal heating was needed to fabricate bilayers and nanostructures in the vast majority of the processes. The direct fabrication of single layers and bilayers of CuO and Cu_2O components have been reported by photoelectrochemical reactions in an aqueous solution without any heating process,[23] and the Cu_2O/CuO bilayer revealed quantum efficiencies of approximately 60% and 90% before and after low-temperature heating, with both the CuO and Cu_2O layers acting as photovoltaic layers.[24]

Here, we report the direct fabrications of CuO-Cu_2O nanocomposites by photoelectrochemical high-frequency potential-switching in an aqueous solution containing copper (II) sulfate hydrate, tartaric acid, and sodium hydroxide. Their structural and energy characteristics were investigated with X-ray diffraction, field emission-scanning electron microscopy, X-ray photoelectron spectroscopy, optical absorption spectra measurements, photoelectron yield spectroscopy, Kelvin probe method, and Mott-Schottky plots measurements.

Experimental Method

The single-layers, bilayer, and nanocomposites of CuO and Cu_2O were fabricated by photoelectrochemical reactions in an aqueous solution containing a 0.3 mol l^{-1} copper (II) sulfate hydrate, 0.3 mol l^{-1} tartaric acid, and 1.5 mol l^{-1} sodium hydroxide at solution pH of 13 by using a potentiostat (IviumStat.h, Ivium Technology). The CuO and Cu_2O components were deposited at 0.4 V and −0.4 V referenced to Ag/AgCl electrode with a Pt counter electrode, and the CuO-Cu_2O nanocomposites were fabricated at 100, 500, and 1000 cycles. The 1 cycle was composed of a combination of the CuO and Cu_2O depositions, and 0.5 cycles would mean the deposition of a single CuO or Cu_2O layer. The CuO/Cu_2O bilayer was expressed as the abbreviation of the CuO/Cu_2O/n-ZnO/FTO substrate fabricated at 1 cycle. The total absolute value of the electric charge was 2 C cm^{-2} for all fabrications, and the electric charge for each unit cycle of CuO and Cu_2O depositions were set at constant values calculated by dividing 2 C cm^{-2} by the number of cycles times two. For example, the deposition charge for a unit cycle was set at 1 mC cm^{-2} for CuO deposition at 1000 cycles. The light irradiation was carried out during the fabrication with a high-pressure Mercury lamp (USHIO, OPTICAL MODULEX, 500 W) without any optical filter. The ZnO layer was prepared by cathodic deposition at −0.8 V vs Ag/AgCl and 333 K in a 0.08 mol l^{-1} zinc nitrate hydrate at an

*Electrochemical Society Member.
[z]E-mail: m-izaki@me.tut.ac.jp

electric charge of 0.5 C cm^{-2} using a potentiostat (HOKUTO DENKO, HAL3000) connected with a coulomb meter (HOKUTO DENKO, HF301). F:SnO_2/soda-lime glass (FTO, AGC Fabritec, Co. Ltd., 10 Ω) was used as the substrate. Prior to the fabrication, the FTO substrates were degreased by anodic polarization at 1 mA cm^{-2} in a 1 mol l^{-1} sodium hydroxide aqueous solution. The solutions were prepared by using reagent-grade chemicals and deionized water purified by Millipore Ellix-UV-Advantage.

X-ray diffraction measurements were performed by RIGAKU RINT2500 with a monochromated CuKα radiation operated at 40 kV and 200 mA. Surface and fractured cross-sectional morphologies were observed with secondary electrons using field-emission scanning electron microscopy (FE-SEM, Hitachi High Technology, SU-8000). Ar ion milled cross sections were prepared at 203 K by using an Ar ion beam accelerating at 4 kV with a cross-section polisher (JEOL Ltd, IB-19530CP), which were observed using a back-scattered electron with FE-SEM (JEOL Ltd, JSM-IT800 〈i〉). The optical absorption spectra were recorded by using a UV–vis-NIR spectrophotometer (Hitachi High Technology, U-4100) with an integrated sphere, and a bare substrate was used as a reference. Electron spectra were recorded with X-ray photoelectron spectroscopy (XPS, ULVAC-PHI Quantera SXM) with a monochromated Al Kα radiation, and the binding energies were corrected referencing the C 1s peak at 284.6 eV. Prior to the measurements, Ar sputtering was performed at an accelerating voltage of 1 kV for 6 s. Ionization energy and work function were measured by using photoelectron yield spectroscopy (PYS) and Kelvin probe method (KP) with APS02, KP Technology. Electrochemical impedance measurements were performed by using Princeton Applied Research, VersaSTAT 4-400 in a 0.1 mol l^{-1} sodium sulfate aqueous solution at pH 6.0 and room temperature, and Mott-Schottky plots were obtained by using software (Princeton Applied Research, VersaStudio).

Results and Discussion

Photoelectrochemical fabrication of CuO-Cu_2O nanocomposites.—Figure 1 shows the chronoamperometry curves for the photoelectrochemical depositions of CuO and Cu_2O single layers, CuO/Cu_2O bilayer, and CuO-Cu_2O nanocomposites at 100 and 1000 cycles. The single CuO and Cu_2O layers were prepared at a cycle number of 0.5 for anodic and cathodic polarizations at 0.4 V and −0.4 V. The CuO/Cu_2O bilayer and CuO-Cu_2O nanocomposites were fabricated by potential switching at cycle numbers of 1, 100, 500, and 1000. The electric charges for each CuO and Cu_2O deposition were kept at constant absolute values of 1 C cm^{-2}, 10 mC cm^{-2}, and 1 mC cm^{-2} at 1, 100, and 1000 cycles since the total electric charge was set constant at 2 C cm^{-2}. The current densities for the depositions of single CuO and Cu_2O layers on the FTO substrate gradually increased and decreased, respectively, reaching a plateau at 0.5 mA cm^{-2}, and −4.3 mA cm^{-2} after the deposition time of 2300 and 220 s. (Figs. 1a, 1b). For the 1-cycle deposition of the CuO/Cu_2O-bilayer fabrication (Fig. 1c), the current density gradually decreased and reached a plateau at −2.86 mA cm^{-2} during the Cu_2O deposition on the same FTO substrate, resembling the single-Cu_2O layer deposition. However, the current density rapidly changed to the anodic side just after the potential was switched from −0.4 V to 0.4 V for the CuO deposition and reached immediately an almost constant value of 0.79 mA cm^{-2} after a remarkable overshooting, which tendency was distinctive from the single-CuO layer deposition on the FTO substrate (Fig. 1b). The deposition time of the CuO and Cu_2O depositions for each absolute electric charge of 1 C cm^{-2} were 1285 s and 121 s, respectively.

In the CuO-Cu_2O nanocomposite fabrication of 100 cycles (Fig. 1d), the behavior of the current density response for the Cu_2O deposition was almost similar throughout the fabrication, and the deposition period for the constant electric charge decreased with the deposition cycle and time, due to the increase in the peak and plateau current densities. The deposition duration and peak current density for the Cu_2O deposition at the 1st and 100th cycles were 28 s, 0.71 mA cm^{-2}, and 4.2 s, −4.5 mA cm^{-2}, respectively. Also, the CuO deposition showed a similar current density response profile composed of overshooting and plateau regions, irrespective of the repeating cycles. The deposition duration decreased while the plateau current density increased with deposition time and cycle, which were 290 s, 0.03 mA cm^{-2}, and 5.9 s, 1.9 mA cm^{-2} at the 1st and 100th cycles respectively. The detailed current density response

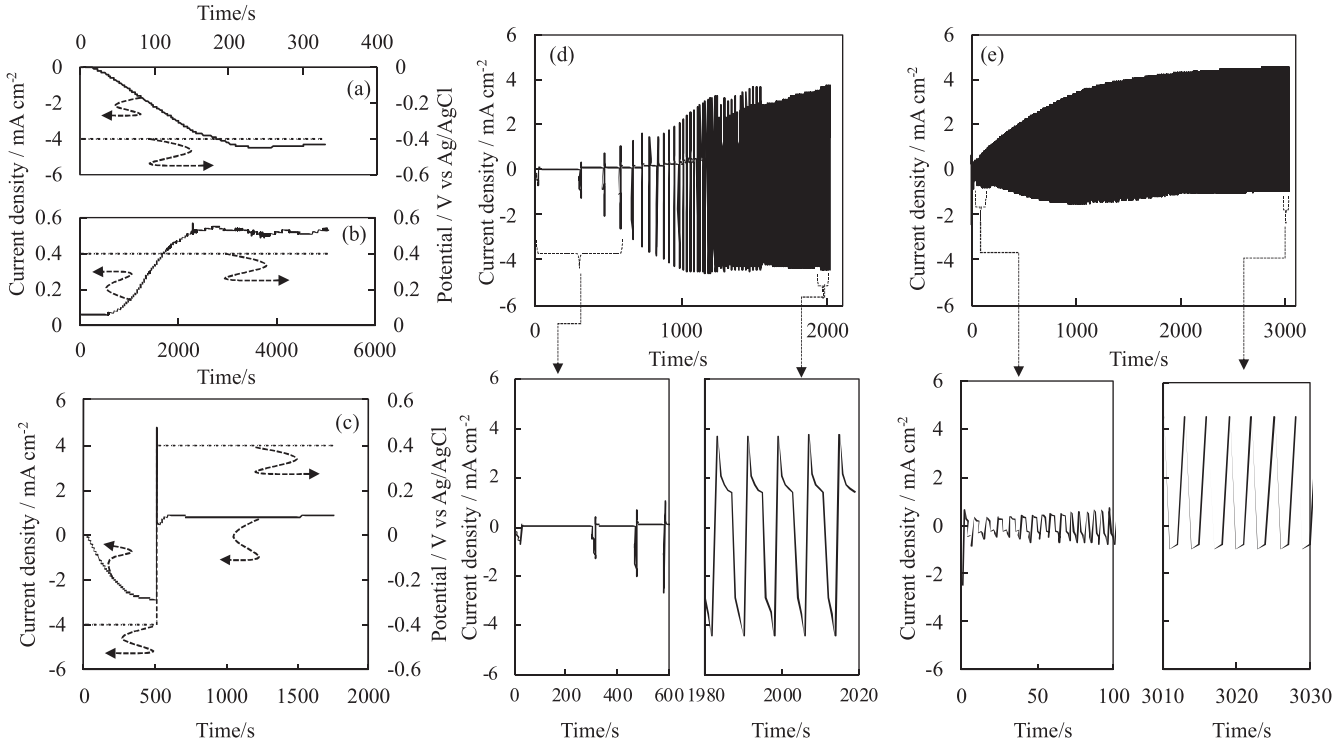

Figure 1. Chronoamperometry curves for fabricating single Cu_2O (a), CuO (b), Cu_2O/CuO bilayer (c), and CuO-Cu_2O nanocomposites (d), (e) by photoelectrochemical potential-switching deposition at 0.5 (a), (b), 1(c), 100 (d), and 1000 (e) cycle.

could not be observed for the 1000-cycle-deposition due to the short deposition periods ranging from 2.9 s to 6.3 s, which were close to the sampling time of 1 s for the measurements. The rough profiles of the current density response were similar irrespective of deposition time or the number of repeating cycles, although the peak anodic current density for the CuO deposition increased with the number of repeating cycles. Nonetheless, the current density response triggered by the potential-switching could be observed, irrespective of the deposition time and total cycle number, even for a very small electric charge of 1 mC cm^{-2} per cycle in the deposition of 1000 cycles.

Figure 2 shows the Cu2p, Cu LMM, and valence band spectra for the single layers, bilayer, and nanocomposites of CuO, and Cu_2O components by XPS measurements. The main peak at 934.2 eV and satellite peak from 939 eV to 944 eV were observed for the single CuO layer and top CuO layer in CuO/Cu_2O bilayer, and the profile and peak energies were the same as that for the CuO layer prepared by heating Cu film in atmospheric oxygen pressure.[25] The single Cu_2O layer showed a peak at 932.5 eV on the Cu2p spectrum, which agreed with the standard value of Cu_2O.[26] The CuO-Cu_2O nanocomposites showed almost the same Cu2p spectra in profile and peak energies, irrespective of the cycle number. The main peak at 933.6 eV was located between the 934.2 eV and 932.5 eV for single CuO and Cu_2O layers, and characteristic satellite peak originated from the CuO component was clearly observed, indicating that the Cu2p spectra for the CuO-Cu_2O nanocomposites were convoluted components of CuO and Cu_2O. The Cu2p spectra could be deconvoluted using a least-square curve fitting method with a mixture of Gaussian and Lorentzian functions on the background,[27] as shown in Fig. S1. Solid lines represent the recorded Cu2p spectra, and the dashed lines represent the profiles of CuO, Cu_2O, and the background. The molar ratio of CuO and Cu_2O components evaluated from the peak area were an almost constant value of 70 ± 4%, and 30 ± 4% for the CuO-Cu_2O nanocomposites fabricated at 100, 500, and 1000 cycles.

The single Cu_2O layer showed a peak at 570.1 eV in binding energy (916.5 eV in kinetic energy) in the Cu LMM spectrum, and the value was close to the reported value of 570.0 eV (916.6 eV in kinetic energy).[26] Both the CuO layers in the single-layer and bilayer showed a peak at 569.0 eV (917.6 eV in kinetic energy) on the Cu LMM spectra, and the value was close to that already reported.[25,26]

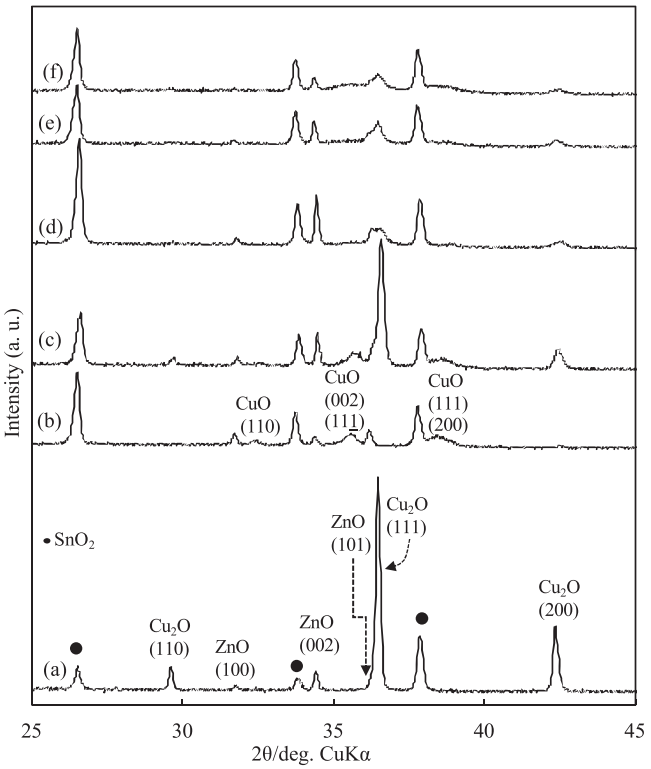

Figure 3. X-ray diffraction patterns for single Cu_2O (a), CuO (b), Cu_2O/CuO bilayer (c), and CuO-Cu_2O nanocomposites by photoelectrochemical potential-switching deposition at 0.5 (a), (b), 1 (c), 100 (d), 500 (e) and 1000 (f) cycles.

The CuO-Cu_2O nanocomposites showed peaks at an almost constant value of 569.8 eV, which were located in between those for the CuO and Cu_2O layers on the Cu LMM spectra (Figs. 6d–6f). From the peak energies and profiles, the Cu LMM spectra for the CuO-Cu_2O nanocomposites were convolutions of the CuO and Cu_2O spectra, like the Cu2p spectra.

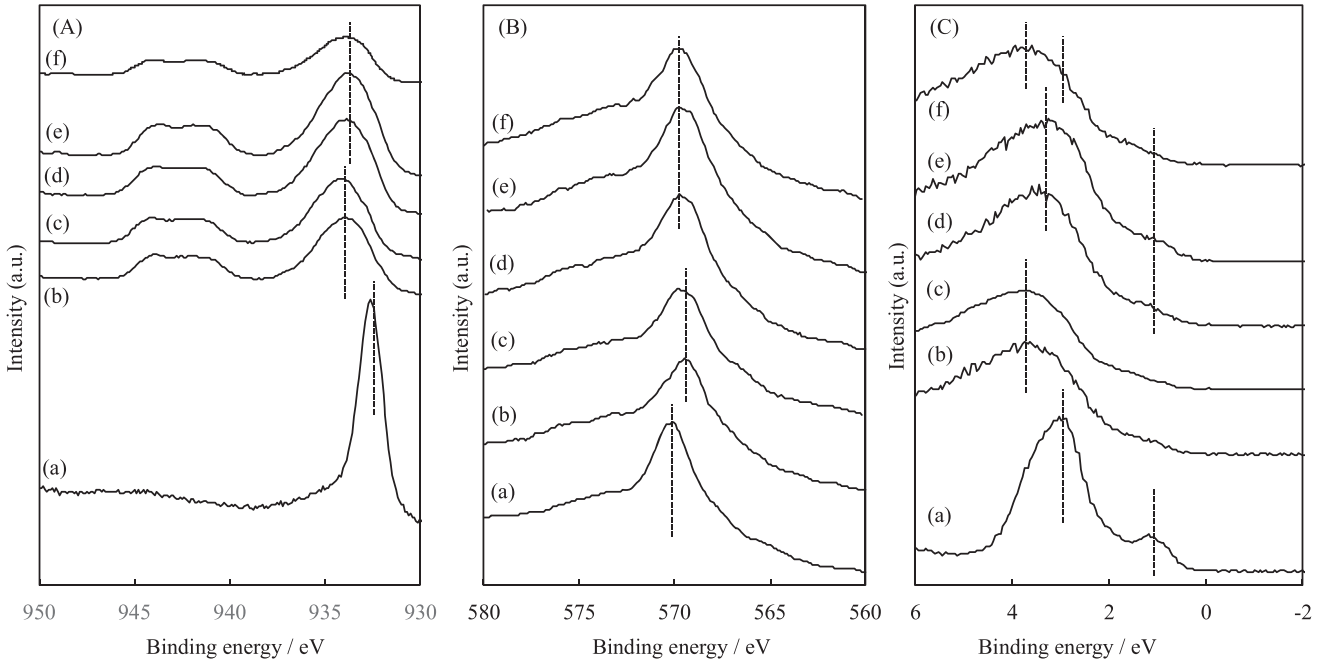

Figure 2. Cu 2p (A), Cu LMM (B), and valence band spectra (C) recorded with XPS for single Cu_2O (a), CuO (b), Cu_2O/CuO bilayer (c), and CuO-Cu_2O nanocomposites (d-f) by 0.5 (a), (b), 1 (c), 100(d), 500 (e) and 1000 (f) cycles photoelectrochemical potential-switching deposition.

The inelastic mean free path of an electron in a solid depends on the kinetic energy.[28] They were roughly estimated to be approximately 400 and 4 atomic layers at binding energies of 1 eV and 500 eV, respectively. Information of the Cu2p and Cu LMM spectra was reflected not only from the surface layer but also from the bulk of the CuO-Cu_2O nanocomposites. The valence band spectra were also measured and will be discussed later.

Figure 3 shows the X-ray diffraction patterns for the single-layers, bilayer, and nanocomposites of CuO and Cu_2O components fabricated at 0.5, 1, 100, 500, and 1000 cycles. The single CuO and Cu_2O layers, denoted as 0.5 cycles, showed their respective diffracted X-ray peaks assigned to CuO with a characteristic monoclinic lattice[29] and Cu_2O with a characteristic cubic lattice.[30] These peaks originated from the CuO and Cu_2O layers could be clearly observed for the CuO/Cu_2O bilayer fabricated as 1 cycle, and there was no change in peak angles and width (full width at half maximum: FWHM) for the peaks of CuO (110), (002), (111) and Cu_2O (110), (111), (200) planes for the single-layers and bilayer of the CuO and Cu_2O components. The intensity of both the CuO and Cu_2O peaks drastically decreased for the CuO-Cu_2O nanocomposites while keeping almost constant peak angles, and the reason was discussed later.

The relation of the FWHM values of CuO (111) and Cu_2O (200) peaks to the cycle number is shown in Fig. S2. The FWHM values for both CuO and Cu_2O components increased with the increase in cycle number, especially over 100 cycles. The FWHM value of the diffracted X-ray peaks mainly originated from grain size broadening and heterogeneous strain broadening, in addition to initial broadening.[31] The increase in FWHM value indicated either the decrease in grain size or an increase in heterogeneous strain for both the CuO and Cu_2O components which constituted the CuO-Cu_2O nanocomposites. The mean grain size (τ) was estimated from the FWHM values (β_τ) by the Scherrer equation as follows:

$$\tau = \frac{0.9\lambda}{\beta_\tau \cdot \cos\theta}$$

where λ and θ represent the wavelength of used X-ray radiation and the Bragg angle. β_τ was obtained by subtracting the instrumental broadening (B_i) from experimentally obtained peak broadening (B).[31] The mean grain size of CuO and Cu_2O components in the CuO-Cu_2O nanocomposite fabricated at 1000 cycles were roughly estimated to be 9 nm and 16 nm, respectively, when peak broadening (B) was mainly attributed to the grain size broadening (β_τ).

The intensity of the Cu_2O (110), (111), and (200) peaks drastically decreased while keeping most peak angles constant, which similar trend was observed for the intensity of CuO (110), (002), and (111) peaks for all the CuO-Cu_2O nanocomposites. The ratio of the intensity of the diffracted line hkl of the phase α in mixture (I_α) to the intensity for pure phase α (I_α^0) is related to the mass fraction (w_α) of phase α by the following equation:[32]

$$\frac{I_\alpha}{I_\alpha^0} = \frac{w_\alpha \left(\frac{\mu}{\rho}\right)_\alpha}{w_\alpha \left\{\left(\frac{\mu}{\rho}\right)_\alpha - \left(\frac{\mu}{\rho}\right)_\beta\right\} - \left(\frac{\mu}{\rho}\right)_\beta}$$

where $\left(\frac{\mu}{\rho}\right)_\alpha$ and $\left(\frac{\mu}{\rho}\right)_\beta$ are respectively the mass attenuation coefficients of phase α and phase β. Since the intensity ratios for both the CuO and Cu_2O components in the CuO-Cu_2O nanocomposites were almost constant irrespective of the cycle numbers, the aforementioned relation of $\frac{I_\alpha}{I_\alpha^0}$ and w_α was applicable to the CuO-Cu_2O nanocomposites. The mass attenuation coefficients of CuO and Cu_2O were calculated to be 44.7 cm^2g^{-1} and 47.9 cm^2g^{-1}, respectively, by using the following equation:

$$\frac{\mu}{\rho} = w_{Cu}\left(\frac{\mu}{\rho}\right)_{Cu} + (1 - w_{Cu})\left(\frac{\mu}{\rho}\right)_O$$

where w_{Cu} is the mass fraction of Cu in CuO and Cu_2O, and $\left(\frac{\mu}{\rho}\right)_{Cu}$ and $\left(\frac{\mu}{\rho}\right)_O$ the mass attenuation coefficients of Cu and O elements, respectively. However, drastic decreases in intensity were observed for both the CuO and Cu_2O components in the CuO-Cu_2O nanocomposites, and there was a possibility the effects of the small grain size contributed to the decrease. The relation of $\frac{I_\alpha}{I_\alpha^0}$

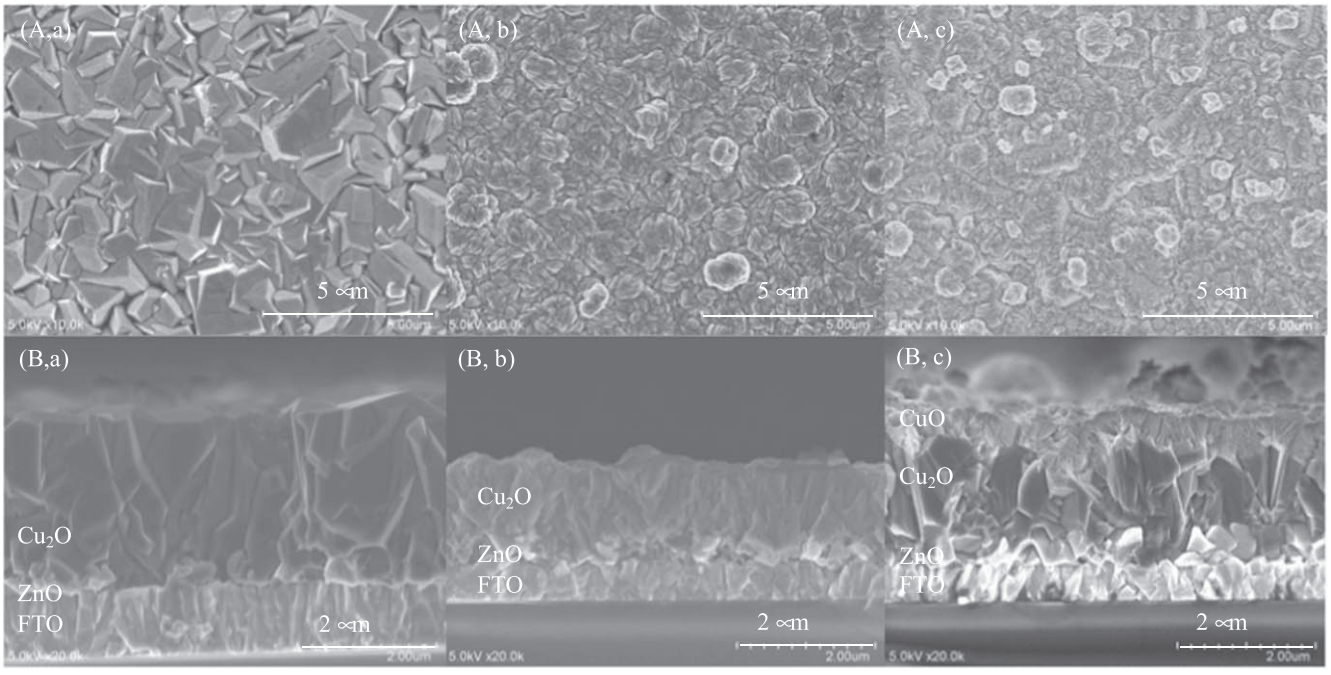

Figure 4. Scanning electron microscopic images of the surface (A) and cross-section (B) of single Cu_2O (a), CuO (b), and CuO/Cu_2O bilayer (c) prepared by 0.5 and 1 cycle photoelectrochemical potential-switching deposition.

and w_α was modified for the CuO-Cu_2O nanocomposites to reduce the effects of the small grain size as follows:

$$\frac{\left(\frac{I_{CuO}}{I^0_{CuO}}\right)}{\left(\frac{I_{Cu_2O}}{I^0_{Cu_2O}}\right)} = \frac{\left[\frac{w_{CuO}\left(\frac{\mu}{\rho}\right)_{CuO}}{w_{CuO}\left\{-\left(\frac{\mu}{\rho}\right)_{CuO}-\left(\frac{\mu}{\rho}\right)_{Cu_2O}\right\}-\left(\frac{\mu}{\rho}\right)_{Cu_2O}}\right]}{\left[\frac{(1-w_{CuO})\left(\frac{\mu}{\rho}\right)_{Cu_2O}}{(1-w_{CuO})\left\{-\left(\frac{\mu}{\rho}\right)_{Cu_2O}-\left(\frac{\mu}{\rho}\right)_{CuO}\right\}-\left(\frac{\mu}{\rho}\right)_{CuO}}\right]}$$

The integrated intensity was used as the intensity of I_α and I^0_α, and the calculation was performed for CuO (111) and Cu_2O (200) peaks. The mass fraction of CuO and Cu_2O in the CuO-Cu_2O nanocomposites were estimated to be approximately 62% and 38%, irrespective of the cycle numbers, and the molar fraction of CuO and Cu_2O components were 74 ± 3% and 26 ± 3%, respectively, which values were consistent with those estimated from the peak deconvolution by XPS. While it remained difficult to precisely tell the fraction of Cu^{1+} and Cu^{2+} states in each CuO and Cu_2O component from the XPS and XRD measurements, it was clear that the CuO content was larger than the Cu_2O content in the CuO-Cu_2O nanocomposites.

The secondary electron images of the surface and cross-section for CuO, Cu_2O single-layers, and CuO/Cu_2O bilayer were shown in Fig. 4. The ZnO layer was located between the FTO substrate and the CuO and Cu_2O layers, and any defects such as pores could not be observed throughout the CuO/ZnO, and Cu_2O/ZnO layers. The single Cu_2O layer was composed of angular columnar grains with a size of approximately 0.5 μm and a length corresponding to a layer thickness of 2.4 μm for the electric charge of 2 C cm^{-2}. The single CuO layer was composed of granular grains approximately 0.16 μm in size, and the thickness was estimated to be approximately 1.2 μm for the deposition of 2 C cm^{-2} electric charge. The CuO/Cu_2O bilayer was a layered structure composed of an upper 0.54-μm-CuO and a lower 1.1-μm-Cu_2O layer, with the grain morphology and size similar to those of single CuO and Cu_2O layers.

Figure 5 shows the secondary electron images of the surface and fractured cross-section for CuO-Cu_2O nanocomposites fabricated at 100, 500, and 1000 cycles, morphologies of Cu_2O and CuO grains fabricated at 100 cycles, and Ar ion milled cross-sectional images for 500 and 1000 cycles. The grain morphologies of the CuO and Cu_2O components drastically changed in the CuO-Cu_2O nanocomposites fabricated at cycle numbers over 100. There were two types of aggregations composed of cubic Cu_2O grains and granular CuO grains on the surface for all the CuO-Cu_2O nanocomposites, as shown in Figs. 5C,d, e. The cubic morphology originated from the characteristic cubic lattice for Cu_2O, indicating that the fabrication condition was close to the equilibrium state.[33] The granular CuO grain was composed of thorn-like smaller grains, and the morphology was similar to those prepared by electrodeposition in a Cu-NH_3 complex aqueous solution.[22] While the equilibrium shape for CuO with a characteristic monoclinic lattice could not be speculated from the complex lattice, the fabrication condition would be close to the equilibrium state, since CuO with a similar thorn-like morphology was formed by thermal oxidation of Cu sheet.[20] The sizes of the Cu_2O grains were estimated to be 44 nm, 22 nm, and 18 nm at 100, 500, and 1000 cycles, respectively. And the granular CuO grains and its comprising thorn-like smaller grains possessed the size of 40 nm and 13 nm, 30 nm and 9 nm, and 19 nm and 7 nm at 100, 500, and 1000 cycles, respectively. The granular CuO and cubic Cu_2O grains were observed partly on the cross-section images for the CuO-Cu_2O nanocomposites fabricated at 100 cycles, but the distinction between the CuO and Cu_2O grain regions proved difficult, resulting in poor information regarding their distribution. The total thicknesses of the CuO-Cu_2O nanocomposites were roughly estimated to be 2.2 μm, 3.0 μm, and 2.1 μm at 100, 500, and 1000 cycles, respectively, and spaces between the grains were observed for all the CuO-Cu_2O nanocomposites, along with the existence of large surface irregularity. The secondary electron provides a high spatial resolution, while the backscattered electron provides elemental information originating from the average atomic number, as shown for the CuO/Cu_2O bilayer in Fig. S3.

The CuO-Cu_2O nanocomposites were a mixture of CuO and Cu_2O aggregations distributed throughout the composite, as can be observed from the compositional contrast in Figs. 5D,b and 5D,c). The CuO aggregation appeared as a darker shade of gray and was composed of granular CuO embedding Cu_2O grains, which were cubic in shape with a lighter appearance. The granular CuO grains showed sizes of 14–18 nm and 11–12 nm at 500 and 1000 cycles, while the sizes of the embedded Cu_2O grains were estimated to be 36–83 nm and 9–10 nm at 500 and 1000 cycles, respectively. Aggregations of Cu_2O were also observed, which were mainly composed of cubic Cu_2O grains, with the space between the Cu_2O grains filled with granular CuO. These Cu_2O grains were slightly smaller than those embedded in the CuO aggregation, which respective sizes were estimated to be 18–30 nm and 9–10 nm at 500 and 1000 cycles. On the other hand, the CuO grains observed from both the CuO and Cu_2O aggregations were almost the same in size. The sizes of CuO and Cu_2O grains are summarized in Table SI. The sizes of granular CuO and cubic Cu_2O grains showed the same dependency on the cycle number, as were those estimated from the surface image observed with secondary electrons. It was confirmed that the increase in the FWHM value of the diffracted X-ray peaks was mainly attributed to the decrease in grain size for both the CuO and Cu_2O components. The formation of the aggregations suggested that in this system, photoelectrochemical growth of both the CuO and Cu_2O grains on the same component could be achieved with relative ease.

The reaction schemes for the anodic CuO and cathodic Cu_2O deposition were speculated as follows:[34]

(AD-i) $2H_2O + 4\,h^+ \rightleftarrows O_2 + 4H^+$
(AD-ii) $[Cu_2(H_{-2}L)_2]^{4-} + 2H^+ \rightleftarrows [Cu_2(H_{-1}L)_2]^{2-}$
(AD-iii) $[Cu_2(H_{-1}L)_2]^{2-} + 4OH^- \rightleftarrows 2Cu(OH)_2 + 2(H_{-1}L)^{3-}$
(AD-iv) $Cu(OH)_2 \rightleftarrows CuO + H_2O$

, and

(CD-i) $[Cu_2(H_{-2}L)_2]^{4-} + 2e\ 2Cu^+ + 2(H_{-2}L)^{4-}$
(CD-ii) $Cu^+ + OH^- \rightleftarrows CuOH$
(CD-iii) $2CuOH \rightleftarrows Cu_2O + H_2O$

The theoretical deposition amounts of CuO and Cu_2O were calculated to be 8.2×10^{-4} g C^{-1}, and 7.4×10^{-4} g C^{-1}, respectively, according to Faraday's law and the reaction schemes. The theoretical thicknesses of the CuO layers were calculated to be 2.6 μm and 1.3 μm at electric charges of 2 C cm^{-2} and 1 C cm^{-2}, respectively, and these values were about twice the experimental values of 1.1 μm and 0.54 μm for the deposition of the single CuO layer and the top CuO layer of the bilayer. Thus, the current efficiency for the CuO deposition was approximated to be 42%. The theoretical thickness values calculated for the Cu_2O deposition were 2.4 μm and 1.2 μm at electric charges of 2 C cm^{-2} and 1 C cm^{-2}, which agreed with the experimental values obtained from the SEM observation, indicating an almost 100% current efficiency. However, it was difficult to estimate the current efficiency for the CuO-Cu_2O nanocomposites because the amount of deposited CuO and Cu_2O components could not be accurately ascertained. The molar ratio of CuO to Cu_2O components in the CuO-Cu_2O nanocomposites was larger than predicted from the current efficiencies of the single layers and bilayer of the CuO and Cu_2O components, suggesting a difference in the growth mechanism of the layer formations.

Energy states of CuO-Cu_2O nanocomposites.—The single-layers and nanocomposites of CuO and Cu_2O components were confirmed to be p-type semiconductors from the negative slopes of

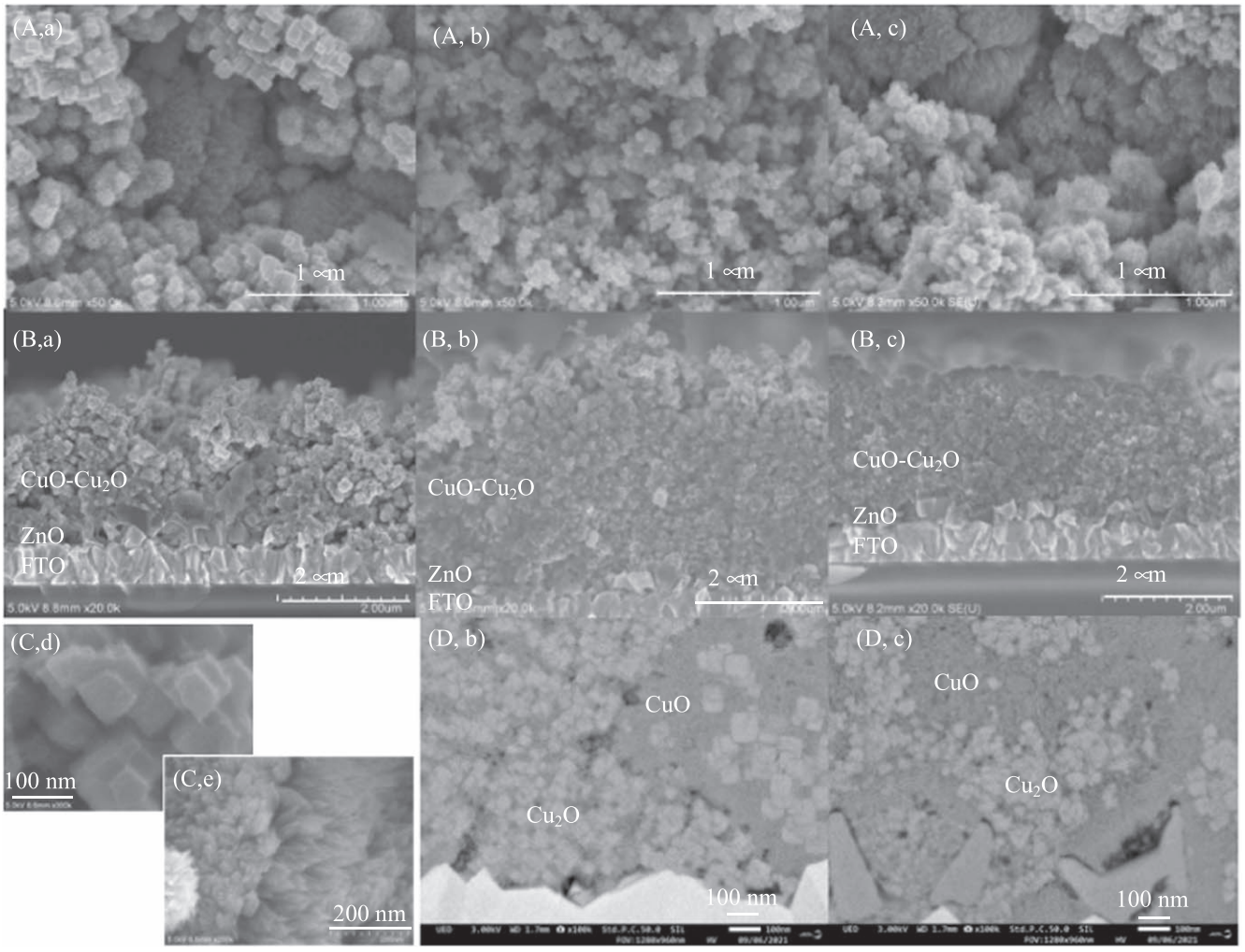

Figure 5. Secondary electron images of the surface (A) and fractured cross-section (B) of CuO-Cu_2O nanocomposites prepared by 100 (a), 500 (b), and 1000 (c) cycles photoelectrochemical potential-switching deposition, and the magnified images (C) for Cu_2O (d) and CuO grains (e) in CuO-Cu_2O nanocomposite fabricated at 100 cycles, and back-scattered electron images of the Ar ion milled cross-section images (D) for 500 (b), and 1000 (c) cycles.

the Mott-Schottky plots as shown in Fig. S4. Figure 6 shows the optical absorption spectra for single-layers, bilayer, and nanocomposites of the CuO and Cu_2O, the relationship between the absorption coefficient and photon energy for the CuO-Cu_2O nanocomposites fabricated at 500 cycles, and the effects of the cycle number on the bandgap energies of CuO and Cu_2O components. The single CuO and Cu_2O layers showed absorption edges around 850 nm and 650 nm in wavelength respectively (Figs. 6Aa, b), while the CuO/Cu_2O bilayer possessed both absorption edges in the spectra (Fig. 6Ac). CuO and Cu_2O are respectively considered to be indirect and direct semiconductors,[21,22] and the relationship between the absorption coefficient (α), and photon energy (E) is as follows:

$$(\alpha h\upsilon)^n \propto (E - E_g)$$

where h, υ, and E_g are Plank constant, the frequency of light, and the bandgap energy. For direct transition, n = 2, while for indirect transition, n = 1/2.[21,22] The bandgap energies were estimated by extrapolating the linear part to the background line, as shown in Figs. 6Bg, 6Bh. The CuO and Cu_2O layers possessed the bandgap energies of approximately 1.5 eV and 2.05 eV, respectively, when deposited as single-layers and as bilayer, agreeing with reported values.[21,22] The CuO-Cu_2O nanocomposites also possessed two absorption edges in the absorption spectra. The absorption edge originating from the CuO component could be mostly observed appearing at a constant wavelength, and the bandgap energy was estimated to be 1.5 eV. The absorption edge of Cu_2O, however, shifted slightly towards a longer wavelength with the increase in the cycle number, with the corresponding bandgap energy decreasing from 2.05 eV to 1.85 eV. While it is known that nanodots and nanoparticles with sizes below 10 nm can exhibit bandgap widening due to the quantum size effect,[35,36] the decrease in the bandgap energy for the Cu_2O components showed that such effect had not taken place, despite the almost corresponding grain size of around 10 nm. The accurate estimation of the amount of the Cu^{2+} state in the Cu_2O component by XPS and XRD proved difficult, but the incorporation of a small amount of Cu^{2+} state may have induced the decrease in the bandgap energy of the Cu_2O layer prepared by electrodeposition.

The valence band spectra for the single-layers, bilayer, and nanocomposites of CuO and Cu_2O components were shown in Fig. 2. The valence band spectrum for the single Cu_2O layer possessed two peaks at 1.09 eV and 2.96 eV, and the energy difference between the Fermi level (E_F) and valence band maxima (E_v) was estimated to be 0.33 eV (Fig. 2a). The valence band spectra for the single CuO and top CuO layers possessed a peak at 3.69 eV, and the energy difference between the Fermi level (E_F) and valence band maxima (E_v) was to be 0.38 eV. The valence band spectra for the nanocomposites of 100 and 500 cycles composed a strong peak at 3.28 eV, which was similarly located between 3.69 eV and 2.98 eV for the CuO and Cu_2O layers, with an additional weak peak at 1.06 eV attributed to the Cu_2O layer. The CuO-Cu_2O

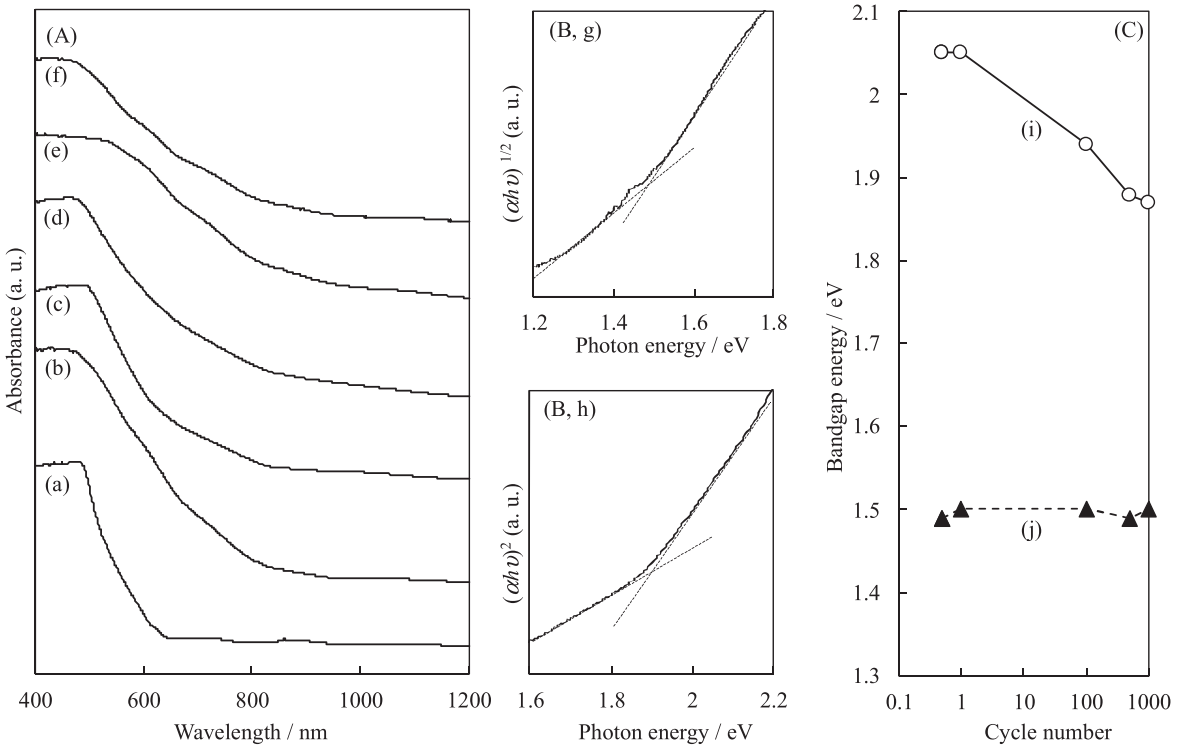

Figure 6. Optical absorption spectra (A) for fabricating single Cu_2O (a), CuO (b), Cu_2O/CuO bilayer (c), and CuO-Cu_2O nanocomposites (d), (e) by 0.5 (a), (b), 1(c), 100 (d), 500 (e) and 1000 (f) cycle photoelectrochemical potential-switching deposition, the relationship (B) between the absorption coefficient and photon energy for indirect (g) and direct transition (h), and the relation between the bandgap energy of Cu_2O (i) and CuO (j) to the cycle number (C).

nanocomposite fabricated at 1000 cycles possessed a strong peak at 3.69 eV corresponding to that for the single CuO layer and a weak peak at 1.06 eV originating from the Cu_2O component. From the peak energies and profiles, the valence band spectra for the CuO-Cu_2O nanocomposites were convolutions of the CuO and Cu_2O spectra, like the aforementioned Cu2p spectra.

The acceptor density (N_A) relates the E_F-E_v value on the valence band spectra as follows;[37]

$$E_F - E_v = \frac{kT}{e} \ln\left(\frac{N_v}{N_A}\right)$$

The effective state density (N_v) was reported to be $5.57 \times 10^{20}\,cm^{-3}$ and $1.1 \times 10^{19}\,cm^{-3}$ for CuO and Cu_2O semiconductors, respectively,[18] and k, T, and e are the Boltzmann constant, temperature, and the electron charge. The acceptor density was estimated to be roughly $1.6 \times 10^{15}\,cm^{-3}$ and $1.5 \times 10^{13}\,cm^{-3}$ for the single CuO and Cu_2O layers, and the value of the Cu_2O layer was in the same order of magnitude as those estimated by a Hall effect measurement for the electrodeposited Cu_2O layer.[38] The CuO-Cu_2O nanocomposites showed acceptor densities of $2.4 \times 10^{16} \sim 5.5 \times 10^{15}\,cm^{-3}$ approximated using the effective state density of the CuO semiconductor.

The ionization energy (IP), work function (ϕ), the energy difference between IP and ϕ(IP-ϕ), and E_F-E_v value are shown in Fig. 7. The ionization energy and work function are defined as the energy differences between the vacuum level and valence band maxima, and between the vacuum level and Fermi level, and the IP-ϕ value is theoretically equal to the value of E_F-E_v. The ionization energy (IP) was estimated to be 5.25 eV and 5.15 eV for the single CuO and Cu_2O layers, and the CuO-Cu_2O nanocomposites possessed ionization energies of 5.18 eV ~ 5.20 eV, which were located between values of single CuO and Cu_2O layers. The work functions (ϕ) were estimated to be 4.73 eV and 4.89 eV for the single CuO and Cu_2O layers, and the CuO-Cu_2O nanocomposites possessed comparatively decreased work functions of 4.69 eV ~ 4.63 eV. The IP-ϕ values showed the same dependency on the cycle number as E_F-E_V values, with slight differences between them. The ionization energy and work function were reported to be 5.2 eV ~ 5.5 eV, 4.7 eV ~ 5.5 eV for CuO semiconductor,[39] and 5.03 eV ~ 5.66 eV, and

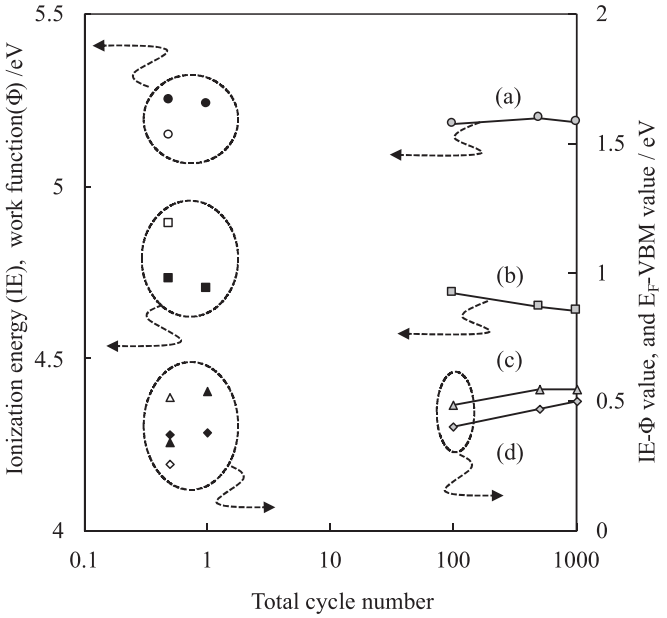

Figure 7. Ionization energy (IE, a), work function(Φ, b), and IE-Φ value estimated from IE and Φ values (c) and E_F-VBM values (d) estimated from valence band spectra shown in Fig. 5 for single Cu_2O (○, □, △, ◊), CuO (•, ■, ▲, ◆), Cu_2O/CuO bilayer, and CuO-Cu_2O nanocomposites by 0.5, 1, 100, 500 and 1000 cycle photoelectrochemical potential-switching deposition. 0.5 cycles indicate the formation of single CuO and Cu_2O layers, and 1 cycle indicates a CuO/Cu_2O bilayer.

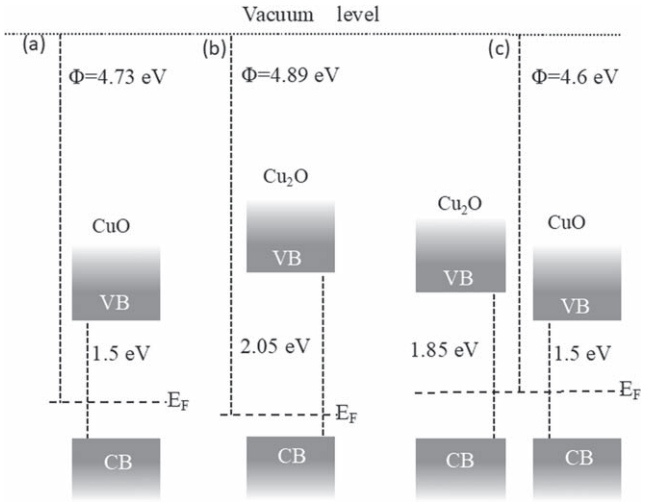

Figure 8. Schematic illustrations of energy band structures of CuO (a), Cu_2O (b), and CuO-Cu_2O nanocomposite semiconductors (c) fabricated at 1000 cycles. E_F: fermi level, Φ: Work function, VB: Valence band, CB: Conduction band

4.74 eV ∼ 5.07 eV for Cu_2O semiconductors,[40] respectively. Figure 8 shows schematic illustrations of energy band structures for CuO, Cu_2O, and CuO-Cu_2O nanocomposite semiconductors fabricated at 1000 cycles. While the location of the Fermi levels depended on the acceptor densities, the ionization energies and work functions reported here were within the range as already reported. The exact reason for the change in the bandgap energy for the Cu_2O components and the change in both the ionization energy and Fermi level in the CuO-Cu_2O nanocomposites were not clear at present, suggesting the need for further investigations including the simulation of their energy band structures.

Conclusions

The p-type CuO-Cu_2O nanocomposite semiconductors composed of Cu_2O-embedded CuO aggregations and Cu_2O aggregation consisting of space-filling CuO grains have been fabricated by photoelectrochemical high-frequency potential-switching at 100, 500, and 1000 cycles in an aqueous solution containing copper (II) sulfate hydrate, tartaric acid, and sodium hydroxide. The CuO and Cu_2O layers were prepared by electrodeposition at current efficiencies of approximately 42% and 100%, respectively. The CuO-Cu_2O nanocomposites were composed of approximately 70 mol% CuO and 30 mol% Cu_2O components, irrespective of the cycle numbers. The increase in the cycle numbers contributed to the decrease in grain size from approximately 40 nm to 7 nm and 44 nm to 9–10 nm for the CuO and Cu_2O components, respectively, in addition to the change in bandgap energy from 2.05 eV to 1.85 eV for the Cu_2O component by the incorporation of Cu^{2+} states, while the bandgap energy of 1.5 eV for the CuO component remained constant. The ionization energy and work function were estimated to be approximately 5.2 eV and 4.6 eV for all the CuO-Cu_2O nanocomposites and were close to the values for the single CuO and Cu_2O layers. This paper provides a fundamental material extending to high-performance photovoltaic layers available to solar cells and photoelectrodes.

Acknowledgments

This work was supported in part by a Grant-in-Aid for Scientific Research (19H02810).

ORCID

Pei Loon Khoo https://orcid.org/0000-0002-4230-6791
Tsutomu Shinagawa https://orcid.org/0000-0001-5671-1512
Masanobu Izaki https://orcid.org/0000-0002-3959-1923

References

1. G. W. Crabtree and N. S. Lewis, *Phys. Today*, **60**, 37 (2007).
2. S. Almosni et al., *Sci. Tech. Adv. Mater.*, **15**, 336 (2018).
3. M. G. Walter, E. L. Warren, J. M. Mckone, S. W. Boettcher, M. Qixi, and E. A. Santori, *Chem. Rev.*, **110**, 6446 (2010).
4. W. Ouyang, F. Teng, J.-H. He, and X. Fang, *Adv. Func. Mater.*, **29**, 1807672 (2019).
5. K. Sivula and R. van de Krol, *Nat. Rev. Mater.*, **1**, 15010 (2016).
6. K. L. Chopra, P. D. Paulson, and V. Dutta, *Prog. Photovol.: Res. Appl.*, **12**, 69 (2004).
7. W. Shockley and H. J. Queisser, *J. Appl. Phys.*, **32**, 510 (1961).
8. M. Yamaguchi, K.-H. Lee, P. Schygulla, F. Dimorth, T. Takamoto, R. Ozaki, K. Nakamura, N. Kojima, and Y. Ohshita, *Energ. Power Eng.*, **13**, 413 (2021).
9. J. F. Geisz, R. M. France, K. L. Shulte, M. A. Steiner, A. G. Norman, H. L. Guthrey, M. R. Young, S. Song, and T. Moriarty, *Nat. Energy*, **5**, 326 (2020).
10. D. W. Snoke, A. J. Shields, and M. Cardona, *Phys. Rev. B*, **45**, 693 (1992).
11. F. P. Koffyberg and F. A. Benko, *J. Appl. Phys. 53*, **1173** (1982).
12. M. Izaki, T. Shinagawa, K. Mizuno, Y. Ida, M. Inaba, and A. Tasaka, *J. Phys. D: Appl. Phys.*, **40**, 3326 (2007).
13. K. Yamamoto, S. Shibasaki, and N. Nakagawa, *Toshiba Rev.*, **74**, 30 (2019).
14. A. Paracchino, V. Laporte, K. Sivula, and M. Gratzel, *Nat. Mater.*, **10**, 456 (2011).
15. M. Izaki, K. Fukazawa, K. Sato., P. L. Khoo, M. Kobayashi, A. Takeuchi, and K. Uesugi, *ACS Appl. Energ. Mater.*, **2**, 4833 (2019).
16. A. A. Dubale et al., *J. Mater. Chem. A*, **3**, 12482 (2015).
17. A.-Y. Kim, M. K. Kim, K. Cho, J.-Y. Woo, Y. Lee, S.-W. Han, D. Byun, W. Choi, and J. K. Lee, *ACS Appl. Mater. Interface*, **8**, 19514 (2016).
18. Y. Yang, D. Xu, Q. Wu, and P. Diao, *Sci. Rep.*, **6**, 35158 (2016).
19. T. Minami, Y. Nishi, and T. Miyata, *APEX*, **9**, 052301 (2016).
20. P. Wang, X. Zhao, and B. Li, *Opt. Exp*, **19**, 11271 (2011).
21. K. Mizuno, M. Izaki, K. Murase, T. Shinagawa, M. Chigane, M. Inaba, A. Tasaka, and Y. Awakura, *J. Electrochem. Soc.*, **152**, C179 (2005).
22. M. Izaki, M. Nagai, K. Maeda, B. M. Fariza, K. Motomura, J. Sasano, T. Shinagawa, and S. Watase, *J. Electrochem. Soc.*, **158**, D578 (2011).
23. M. Izaki, P. L. Khoo, and T. Shinagawa, *J. Electrochem. Soc.*, **168**, 112510 (2021).
24. M. Izaki, S. Abe, K. Nakakita, and P. L. Khoo, *ACS Omega*, **6**, 27587 (2021).
25. J. Haber, T. Machel, L. Ungier, and J. Ziolkowski, *J. Solid State Chem.*, **25**, 207 (1978).
26. J. F. Moulder, W. F. Sticle, P. E. Sobol, and K. D. Bomben, *Handbook of X-ray Photoelectron Spectroscopy* (Minnesota)(Perkin-Elmer Corporation)p. 86 (1992).
27. D. Briggs and M. P. Seah, *Auger and X-ray Photoelectron Spectroscopy* (New York)(Wiley, Chichester)p. 555 (1990).
28. M. P. Seah and W. A. Dench, *Surf. Interface Anal.*, **1**, 2 (1979).
29. Joint Committee on Powder Diffraction Standards, *Powder Diffraction File* (International Data for Diffraction Data, Swarthmore, PA)5 (1992).
30. Joint Committee on Powder Diffraction Standards, *Powder Diffraction File* (International Data for Diffraction Data, Swarthmore, PA)2 (1992).
31. R. Jenkins and R. L. Snyder, *Introduction to X-ray Powder Diffractometry* (New York)(Wiley)p. 89 (1996).
32. R. Jenkins and R. L. Snyder, *Introduction to X-ray Powder Diffractometry* (New York)(Wiley)p. 355 (1996).
33. M. J. Siegfried and K. S. Choi, *Angew. Chem. Int. Ed.*, **44**, 3218 (2005).
34. M. Izaki, T. Koyama, P. L. Khoo, and T. Shinagawa, *ACS Omega*, **5**, 683 (2020).
35. G. E. Semonin, J. M. Luther, and M. C. Beard, *Mater. Today*, **15**, 508 (2012).
36. S. Baskoutas and A. F. Terzis, *J. Appl. Phys.*, **99**, 013708 (2006).
37. S. M. Sze and K. K. Ng, *Physics of Semiconductor Devices* (New Jersey)(Wiley)p. 45 (2007).
38. T. Shinagawa, M. Onoda, B. M. Fariza, J. Sasano, and M. Izaki, *J. Mater. Chem. A*, **1**, 9182 (2013).
39. J. Morasch, H. F. Wardengs, W. Jaegermann, and A. Klein, *Phys. Status Solidi a*, **213**, 1615 (2016).
40. J. Deuermier, J. Gassmann, J. Brotz, and A. Klein, *J. Appl. Phys.*, **109**, 113704 (2011).